Journal of the Meteorological Society of Japan

EARLY ONLINE RELEASE

The DOI for this manuscript is
DOI:10.2151/jmsj.2024-002
J-STAGE Advance published date: September 27th, 2023

Optical Properties of Aerosol Particles in the Atmospheric Boundary Layer over the Northwestern Pacific: High Refractive Index for Coarse Particles in Pristine Air

Seizi KOGA[1]

Current affiliation, *Branding and Public Relations Department*
Former affiliation, *Environmental Management Research Institute*
National Institute of Advanced Industrial Science and Technology, Tsukuba, Japan

Sep. 13, 2023

---

1) Corresponding author: Seizi Koga, Branding and Public Relations Department, National Institute of Advanced Industrial Science and Technology, AIST Tsukuba, 1-1-1, Umezono, Tsukuba, Ibaraki 305-8560 JAPAN
E-mail, koga-s@aist.go.jp
Tel: +81-29-861-8388

Abstract

To determine the complex refractive indices of aerosol particles in the atmospheric boundary layer, simultaneous measurements of scattering coefficients at 450, 550, and 700 nm wavelengths, absorption coefficient at 565 nm, and aerosol particle number size distributions were performed during a voyage of the icebreaker *Shirase* from Tokyo to the offing of the Philippines over the northwestern Pacific in November 2010. Three sets of Ångström exponents were calculated using the three observed scattering coefficients. Using the observed number size distributions, three sets of Ångström exponents were reproduced by assuming their complex refractive indices. Appropriate complex refractive indices for aerosol particles in the atmospheric boundary layer can be obtained when the difference between the observed and reproduced Ångström exponents is minimal. Absorbing substances were assumed to be present in the fine particles. For polluted air masses, if the refractive index for aerosol particles was uniform regardless of the particle size, the estimated Ångström exponents were consistent with the observed values. The refractive index must be the normal dispersion, which increases with a decrease in wavelength. For pristine air masses, the refractive index was estimated to be higher for coarse particles than for fine particles. This could be explained by preferential condensation of organic compounds onto coarse particles, which is observed to alter the number size distribution over Chichi-jima of the Ogasawara Islands in the northwestern

Pacific in August 2014 and February 2015. This study is the first to report that the increase in the refractive index of coarse particles is likely caused by the optical properties of volatile organic compounds and/or secondary organic aerosols condensed on coarse particles.

Keywords complex refractive index; scattering coefficient; Ångström exponent; secondary organic aerosol; number size distribution

1. Introduction

New aerosol particles are generally formed by the nucleation of aerosol particles with diameter $D < 0.01$ μm (Kulmala et al., 2004). Number size distributions in the Aitken ($0.01 < D < 0.1$ μm) and accumulation ($0.1 < D < 1$ μm) modes change when vapor compounds condense onto pre-existing aerosol particles or evaporate from the particles to the gas phase, and when particles coagulate (Heintzenberg et al., 2003; Kulmala et al., 2004; O'Dowd et al., 2010; Dall'Osto et al., 2012). The chemical composition of coarse particles ($D > 1$ μm) generally differs from that of fine particles ($D < 1$ μm) (Hinds, 1999; Heintzenberg et al., 2003). Matsumoto et al. (1998) investigated the seasonal characteristics of the chemical composition of aerosol particles on Haha-jima (26°38'N, 140°10'E) of the Ogasawara Islands in the northwestern Pacific and determined that sea salt and non-sea salt sulfates (nss–SO_4^{2-}) were the primary chemical species in coarse and fine particles, respectively. This is supported by the results of other studies (Campuzano-Jost et al., 2003; Heintzenberg et al., 2003).

Dimethylsulfide (DMS) is produced by marine phytoplankton and emitted from the ocean to the atmosphere. Its oxidation products in the atmosphere are then converted to sulfuric acid (H_2SO_4), making DMS the most important precursor of nss–SO_4^{2-} in aerosol particles over the ocean (Savoie and Prospero, 1982; Bates et al., 1992; Koga and Tanaka, 1999; Read et al., 2008; Mahajan et al., 2015). However, the observed H_2SO_4 mixing ratios are insufficient for binary nucleation of H_2SO_4 and H_2O (Weber et al., 1999). Using binary

and ternary (H_2O–H_2SO_4–NH_3) nucleation theories, Pirjola et al. (2000) analyzed the possibility of particle formation in the atmospheric boundary layer and found that the formation of new particles is difficult under typical atmospheric conditions. Hence, they proposed the existence of condensable species other than H_2SO_4.

Novakov and Penner (1993) found that natural organic compounds exist in aerosol particles with $0.05 < D < 0.2$ μm. In addition, O'Dowd et al. (2004) suggested that the organic fraction of the mass concentration of fine particles over the North Atlantic Ocean is related to biological activity. Oxidation products of volatile organic compounds (VOC) emitted by phytoplankton (e.g., biogenic amines, isoprene, and monoterpenes) can form secondary organic aerosols (SOA) (Facchini et al., 2008; Gantt et al., 2009; Shaw et al., 2010; Bikkina et al., 2014). The enrichment of water-soluble organic carbon (WSOC) in aerosol particles can be explained by the production and condensation of SOA in pristine air masses (Ceburnis et al., 2008; Miyazaki et al., 2010; Decesari et al., 2011). The presence of WSOC probably affects the optical properties of aerosol particles.

Atmospheric aerosol particles scatter and absorb incident sunlight (IPCC, 2013). The optical properties of aerosols are expressed as the scattering coefficient σ_{scat} and absorption coefficient σ_{abs} (Seinfeld and Pandis, 1998; Hinds, 1999). Single-scattering albedo (*SSA*), defined as the ratio of σ_{scat} to σ_{ext} ($\sigma_{scat} + \sigma_{abs}$), is an important factor in determining warming or cooling in the atmosphere–surface system (Srivastava et al., 2020). Incident sunlight is scattered mainly by sulfates (SO_4^{2-}) in aerosol particles (Shiobara et al., 2007; Ohta et al.,

100 2013). Aerosols, including elemental carbon and soil, absorb sunlight (IPCC, 2013).
101 Elemental carbon is emitted from anthropogenic sources into the atmosphere (Bond and
102 Bergstrom, 2006; Bond et al., 2013). The scattering and absorption coefficients of individual
103 aerosol particles are associated with the complex refractive index m (n, k) = $n - ki$ of the
104 chemical composition of the aerosol particle. The real part, n, of m (n, k), represents the
105 phase velocity of the electromagnetic wave propagating through the medium. The imaginary
106 part, k, represents the attenuation rate of the amplitude of the propagating electromagnetic
107 wave. The optical properties of aerosol particles are determined by their size-dependent
108 chemical composition and number size distribution. The value of m (n, k) depends not only
109 on the medium, but also on the wavelength of the electromagnetic wave (Bohren and
110 Huffman, 1998).

111 Koga (2021) reported aerosol optical properties in the atmospheric boundary layer over
112 the northwestern Pacific and Southern Ocean during the 52nd Japanese Antarctic Research
113 Expedition (JARE52) voyage from November 11, 2010, to March 17, 2011. The present
114 study focuses on the m (n, k) of aerosol particles in polluted and pristine air masses over
115 the northwestern Pacific. The purpose of this study is to estimate the m (n, k) of aerosol
116 particles in two types of air masses using observed aerosol scattering and absorption
117 coefficients and number size distributions. This study also reports that the estimated high n
118 value of the coarse particles in pristine air masses is likely caused by the optical properties
119 of SOA condensed on coarse particles.

120 Results reinforcing this idea were obtained from observations of aerosol number size
121 distributions using an activated carbon fiber on Chichi-jima (27°04'N, 142°13'E) of the
122 Ogasawara Islands in the northwestern Pacific in 2014 and 2015. These observations were
123 designed to elucidate why aerosol number size distributions differ between polluted and
124 pristine air masses. When condensable species are added to the atmosphere, the formation
125 of new particles and change in number concentration occur mainly in the fine particle range.
126 However, the results of observations on Chichi-jima suggest that some volatile substances
127 condense onto coarse particles in pristine air masses.
128 The estimation of the m (n, k) of aerosol particles during the JARE52 voyage and the
129 observations on Chichi-jima provide some insight into the optical properties of the coarse
130 particles.
131
132 **2. Observations**
133 To be able to determine the appropriate m (n, k) for aerosol particles, the present
134 study used the optical properties and number size distributions obtained during the JARE52
135 voyage. To elucidate the difference in the number size distribution between polluted and
136 pristine air masses, observations were conducted on Chichi-jima. Details of these
137 observations are described below.
138
139

140 *2.1. Northwestern Pacific*

141 Fig. 1 shows the JARE52 voyage track of the icebreaker *Shirase* from Tokyo, Japan
142 (35°39'N, 139°46'E) to the Philippines (12°14′N, 129°16′E) in November 2010. Solid curves
143 represent backward trajectories for the preceding 3 d of air parcels at a 500 m altitude. Open
144 circles on the track indicate the vessel positions every 6 h. These trajectories were computed
145 using the hybrid single-particle Lagrangian integrated trajectory (HYSPLIT) model (Stein et
146 al., 2015; Rolph et al., 2017) based on the vertical velocity data fields from the NCEP/NCAR
147 reanalysis data.

148 The aerosol scattering coefficients (σ_s^{λ}, m^{-1}) were measured by a 3563-model
149 integrating nephelometer at three wavelengths: 450, 550, and 700 nm (3563-IN, TSI Inc.
150 Shoreview, MN). The σ_s^{λ} measurements were repeated at intervals of 1 min during the
151 voyage. The aerosol absorption coefficients (σ_{PSAP}, m^{-1}) were measured at intervals of 1
152 min using a particle soot absorption photometer (PSAP; Radiance Research, Seattle, WA).

153 The 3563-IN and PSAP methods have errors due to the measurement principle.
154 Correction factors (C^{λ}) are linear functions of Ångström exponents (*AE*) calculated using
155 uncorrected σ_s^{λ} values of two specific wavelengths (Anderson and Ogren, 1998). In the
156 present study, the C^{λ} values, which were within the ranges estimated by Anderson and
157 Ogren (1998), were applied to obtain the corrected σ_{ts}^{λ} values for the uncorrected σ_s^{λ} values
158 (Table 1). Using the σ_{ts}^{λ} of two wavelengths, for example, a value of *AE* between 450 and
159 550 nm is defined as:

$$AE_{450-550} = -\frac{\log(\sigma_{ts}^{450}/\sigma_{ts}^{550})}{\log(450/550)}. \quad (1)$$

In the PSAP, scattering compounds on the filter could lead to the overestimation of the absorption coefficients. To volatilize the scattering compounds, the sample air was maintained at 300 °C. The airflow rate measured using the built–in pump and in the sample spot area has uncertainties (Bond et al., 1999). The correction factors for these uncertainties were applied to obtain corrected σ_a values for the σ_{PSAP} values, which led to the decrease of approximately 9.7% of the σ_{PSAP} values (Koga, 2021). The wavelength of 565 nm of light emitted from an LED in the PSAP was different from the wavelength of 550 nm emitted from a quartz-halogen lamp in the 3563-IN. However, the difference between σ_{ts}^{550} and σ_{ts}^{565} was negligible. Thus, the values of σ_{ts}^{550} and σ_a were immediately used to determine *SSA*. The measurements and correction methods for σ_{ts}^{λ} and σ_a are reported in Koga (2021).

The number size distributions of aerosol particles with $D > 0.3$ μm were measured using an optical particle counter (OPC, KC–01D, RION Co., LTD). The light source of the OPC is a semiconductor laser that emits light at a wavelength of 780 nm. Measurements were repeated every 1 min and categorized into five classes: $D > 0.3$ μm, $D > 0.5$ μm, $D > 1$ μm, $D > 2$ μm, and $D > 5$ μm. The OPC was calibrated by the manufacturer using polystyrene latex (PSL) particles with m (1.595, 0). The coefficients of variation (σ/x, that is, sample standard deviation/arithmetic mean) were calculated using a 15 min moving average in the number concentrations of $D > 0.3$ μm. When the coefficients of variation were > 0.25 at a certain time, the values of all classes at that time were excluded.

Fig. 2 displays the σ_{ts}^{λ}, σ_a, and *AE* from Tokyo to the offing of the Philippines, which corresponds to part of the latitudinal distributions of aerosol optical properties from Tokyo to Fremantle (32°03′S, 115°45′E) in Australia, as shown in Koga (2021). The backward trajectories suggest that the air masses from 35.5°N to 28.1°N contained anthropogenic pollution from East Asia. Meanwhile, from 25.3°N to 12.2°N were pristine air masses from the central North Pacific unaffected by anthropogenic pollution (Fig. 1). Fig. 3 shows the time series of number size distributions in four classes reported by the OPC from 30.5°N and 137.5°E to the offing of the Philippines. Relatively stable values were found from 30.5°N to 29.5°N in the polluted air masses, and from 17.5°N to 16.0°N and 14.5°N to 13.5°N in the pristine air masses. The complex refractive indices of aerosol particles were estimated for these latitudinal ranges.

Fig. 4 shows the number size distributions averaged from 30.5°N to 29.5°N and from 17.5°N to 16.0°N. The averages and one standard deviations of C^{λ}, σ_{ts}^{λ}, σ_a, and *SSA* for three latitudinal ranges are listed in Table 1. The standard deviation values of *SSA* were calculated using law of propagation of errors. The *AE* values were calculated from the averages of σ_{ts}^{λ}. The *r* values are correlation coefficients between σ_{ts}^{450} and σ_{ts}^{550}, σ_{ts}^{450} and σ_{ts}^{700}, and σ_{ts}^{550} and σ_{ts}^{700}.

200 *2.2. Chichi-jima of the Ogasawara Islands*

201 Chichi-jima is located approximately 1000 km south of Tokyo, Japan and is an ideal site
202 for monitoring both polluted air masses from East Asia during winter and pristine air masses
203 from the central North Pacific during summer (Koga et al., 2008), which correspond to the
204 first and second types during the JARE52 voyage, respectively (Koga, 2021). The island is
205 located downwind of polluted air masses and upwind of pristine air masses relative to the
206 JARE52 voyage track.

207 Observations were conducted at the Ogasawara downrange station (27°04'N,
208 142°13'E, 230 m above sea level) of the Japan aerospace exploration agency. The number
209 size distribution with D > 0.3 μm was measured using an optical particle sizer (OPS,
210 Model3330, TSI Inc., Shoreview, MN). Measurements were repeated every 1 min. To
211 remove aerosol particles with D > 10 μm, a PM_{10} impactor was attached to an air inlet port
212 with a 4.25 cm inside diameter on the wall of a facility for switchboard equipment. A stainless
213 steel sampling probe was inserted into the inlet pipe and aligned parallel to the gas
214 streamlines made with an air pump. Aerosol sampling was done isokinetically. The inside
215 diameter of the sampling probe was 1.47 cm at the upper end, decreasing gradually to a
216 minimum of approximately 0.64 cm (1/4 inch) at a 7 cm distance.

217 The amount of VOCs condensed onto aerosols can be evaluated from the difference in
218 the number size distributions between VOC-removed and untreated air samples. Kynol
219 (novoloid)-based activated carbon fabric (ACC507-20, Gunei Chemical Industry Co., Ltd.,

220 Gunma, Japan) was inserted into a 50 cm stainless steel tube with an outside diameter of
221 1.27 cm (1/2 inch). The inside diameter of this tube was approximately 0.64 cm (1/4 inch)
222 because Kynol fabric was placed along the inner wall. The inside diameter was the same as
223 the fit diameter of the conductive tubing for the piping to avoid steps in the flow path. Kynol
224 fabric can adsorb non-polar substances such as organic compounds (nominal toluene
225 adsorption, 30–80 w%) but it cannot or poorly adsorbs polar substances such as water vapor
226 (Sullivan et al., 2007). Kynol fabrics are superior to granular activated charcoal in terms of
227 adsorption rate and amount. The stainless steel tube with the Kynol fabric was connected
228 to the upper stream of the OPS to remove VOCs from the air samples.

229 In August 2014, two OPSs were simultaneously used to measure number size
230 distributions, but the Kynol tube was connected to only one of these. The flow splitter (Model
231 3708, TSI Inc.) was used to divide air samples into two flow paths. After the measurement
232 started, the values obtained by the two OPSs became almost identical within 2 h because
233 Kynol fabrics were saturated with VOCs. Judging from this result, particle loss by the Kynol
234 tube is negligible. The saturated Kynol was regenerated as a result of VOC desorption by
235 heating the tube for 30 min at 100 °C with an airflow rate of 20 L min^{-1}. In February 2015,
236 only one OPS was available, and therefore measurements were taken alternately by
237 connecting and disconnecting the Kynol tube.

238 Fig. 5 shows the number and surface area size distributions in the pristine air masses
239 in summer and polluted air masses in winter, obtained using the OPS. The dew point

240 temperatures in the ambient atmosphere were 27 °C on August 22, 2014, and 12 °C on
241 February 18, 2015. The inlet temperature recorded by the OPS, 38 °C in August and 33 °C
242 in February, was consistently higher than the dew point temperature. The relative humidity
243 inside the OPS was estimated to be 54% in August and 29% in February. The number size
244 distributions were obtained under dry conditions.

245 The distinct maxima of the number concentrations were always approximately 2–3 μm
246 in diameter during summer. When the Kynol tube was used, the number concentrations of
247 coarse particles always showed a sharp decrease from the original concentrations. In
248 contrast, the number concentrations in winter decreased with increasing diameter, with an
249 inflection point of approximately 1–2 μm in diameter. The number size distributions, however,
250 hardly changed despite the use of a Kynol tube.

251

252 **3. Methods**

253 Three sets of *AE* were calculated using the three observed σ_{ts}^{λ}. Using the observed
254 number size distributions, the values of σ_{ts}^{λ}, σ_a, and *AE* were reproduced by assuming
255 complex refractive indices. The procedure for reproducing the values of σ_{ts}^{λ} and σ_a is shown
256 below. Appropriate complex refractive indices for aerosol particles in the atmospheric
257 boundary layer can be obtained when the sum of the three sets of differences between the
258 observed and reproduced *AE* is minimal.

259

3.1. Refractive index correction of the particle sizing in the OPC

The particle sizing diameters are based on the threshold voltage from the photodetector receiving light scattered by the PSL particles. In the ambient atmosphere, m (n, k) for aerosol particles is different from that for PSL particles. The particle sizing diameters must be corrected according to the values of m (n, k) to obtain realistic values for the number size distributions.

The photodetector in the OPC was placed at an angle ψ of 70° to the irradiated optical axis. The scattered light was focused by the collecting aperture with a semi-angle β of 27°. The angular distribution of light scattered by a single particle with diameter D was calculated from 43° ($\theta = \psi - \beta$) to 97° ($\theta = \psi + \beta$) at intervals of 1° using the geometry of the collecting aperture by Hodkinson and Greenfield (1965). The range of particle diameters covered by the calculation was from 0.05 to 25 μm, dividing into 1000 increments on a logarithmic scale. For each particle diameter, the total intensity of light received by the photodetector was calculated as the sum of the scattered light intensity per 1° from 43° to 97°. The same procedure was repeated for n from 1.30 to 1.70 in increments of 0.01. As a result, the particle sizing diameters of the 41 sets were obtained as a function of n at a wavelength of 780 nm from the laser light in the OPC.

280 *3.2. Expansion of number size distribution*

281 For the size range between log$D$ and log$D$ + $d$log$D$, the number size distribution n (log

282 D) can be expressed by a power-law function of size as follows:

283 $$n(\log D) = \frac{dN}{d\log D} = cD^{-b}, \qquad (2)$$

284 where N is the number concentration, D is the particle diameter, c is a proportionality

285 constant, a factor that determines the number concentration, and b is the slope of the

286 number size distribution on a log–log plot.

287 The values from N_4 to N_8 in Fig. 6 averaged from 30.5°N to 29.5°N in the polluted air

288 masses and was originally obtained using the OPC. The boundaries from D_4 to D_8

289 corresponded to the original boundaries for m (1.595, 0) of the PSL particles. The values of

290 N_i represent the number concentration at the midpoint between D_i and D_{i+1}. Equation (2) is

291 available between D_i and D_{i+1}, where b_i and c_i are defined in the same diameter range.

292 The observed number size distribution from D_4 to D_8 alone was insufficient to reproduce

293 σ_{ts}^{λ} and σ_a. Therefore, for particles with $D < D_4$, the widths from D_1 to D_2, D_2 to D_3, and D_3

294 to D_4 were assumed to be the same as the width I from D_4 *to* D_5. To obtain the upper limit

295 D_9, the width L from D_7 *to* D_8 was applied to that from D_8 *to* D_9. The slope of the red line

296 between N_2 at D_3 and N_4 was assumed to be the same as that between N_4 and N_5. The N_1

297 value was the same as the N_3 value.

298 All N_i were multiplied by an adjustable factor df to reproduce the same values as the

299 observed σ_{ts}^{λ} and σ_a values. This probably corresponded to the correction for the uncertainty

300 in the airflow rate of the internal pump of the OPC. The values from N_4 to N_8 in Fig. 6 are
301 original values from the OPC in the case of df = 1. The value of df had no effect on the value
302 of AE. The N_3 value at the midpoint between D_3 and D_4 was further multiplied by an
303 adjustable factor sf to obtain AE values consistent with the observed values because the AE
304 values depend on the slope of the number size distribution.

305 The values of N_1 and N_2 were automatically determined using this operation. For
306 example, in the cases of sf = 1.0 and 0.3, the number size distributions are shown by the
307 red and blue lines in Fig. 6, respectively. Henceforth, the number size distribution consisting
308 of black and blue solid lines will be referred to as a column model. The values of D_i were
309 obtained as the particle sizing corrected by m (n, 0). The k values were determined such
310 that the estimated σ_a values were consistent with the observed σ_a values.

311 To confirm the reliability of m (n, k) estimated using the column model, the σ_{ts}^{λ} and σ_a
312 values were reproduced using the regression curves fitted to the column model. The
313 regression curves can be described as the sum of two log-normal distributions (Jaenicke,
314 1993, Seinfeld and Pandis, 1998):

315 $$\frac{dN}{d\log D} = \sum_{j=1}^{2} \frac{N_j}{\sqrt{2\pi}\log\sigma_j} \exp\left(-\frac{\left(\log D - \log D_j\right)^2}{2\log^2\sigma_j}\right), \qquad (3)$$

316 where N_j is the number concentration, σ_j is the standard deviation of the lognormal
317 distribution, and D_j is the mean diameter. Henceforth, the number size distribution consisting
318 of the regression curves will be referred to as a log-normal model.

Clarke et al. (2004) and Koga et al. (2008) reported that most of black carbon was present in fine particles with D < 1 μm. Therefore, the light-absorbing component was only present in the fine particles with D < the corrected D_6 (Fig. 6) in the column model and in the first log-normal distribution (j = 1 in Eq. (3)) in the log-normal model.

3.3. Estimations of σ_{ts}^{λ}, σ_a, and m (n, k)

The scattering coefficient σ_{ts}^{λ} in the particle size range of Mie scattering can be expressed by a power-law function of the wavelength (Seinfeld and Pandis, 1998):

$$\sigma_{ts}^{\lambda} = \int \frac{\pi D^2}{4} Q_{ts}^{\lambda}(m, x) n(\log D) d \log D \propto \lambda^{-AE}, \quad (4)$$

where $Q_{ts}^{\lambda}(m, x)$ is the scattering efficiency of a particle with m (n, k), x is the size parameter defined by the ratio of the particle diameter D to the wavelength of light (λ), n (log$D$) is the number size distribution, and AE was calculated from Eq. (1). A similar expression can be written for σ_a in terms of the absorption efficiency, $Q_a(m, x)$, of the particle with m (n, k). The values of n (log$D$) can be obtained from Eqs. (2) or (3).

The values of $Q_{ts}^{\lambda}(m, x)$ at the three wavelengths, 450, 550, and 700 nm, and $Q_a(m, x)$ at a wavelength of 550 nm were calculated for each particle diameter divided into 1000 increments from 0.05 to 25 μm on a logarithmic scale. The values of n range from 1.30 to 1.70 in increments of 0.01. Q terms were computed from Mie theory using MieCalc software by Bernhard Michel.

The values of *AE* observed by 3563-IN were expressed as the oAE_1 between 450 and 550 nm, oAE_2 between 450 and 700 nm, and oAE_3 between 550 and 700 nm. The values of *AE* from σ_{ts}^{λ} estimated using Eq. (4) were expressed as eAE_1 between 450 and 550 nm, eAE_2 between 450 and 700 nm, and eAE_3 between 550 and 700 nm, respectively. In the estimations of eAE_i, the values of *k* were assumed to be constant regardless of the wavelength of light. The appropriate *m* (*n*, *k*) for aerosol particles can be obtained when the following Eq. (5) is minimized:

$$p = \sum_{i=1}^{3} (oAE_i - eAE_i)^2. \qquad (5)$$

4. Results

4.1. Complex refractive indices of aerosol particles in polluted air masses

The σ_{ts}^{λ} values observed at each wavelength from 30.5°N to 29.5°N were reproduced using the corrected number size distribution of the column model. Here, *k* = 0 in the calculation of σ_{ts}^{λ} using Eqs. (2) and (4) was assumed to simplify the determination of an appropriate *n* value. Values of *p* are shown as a function of *m* (*n,* 0) in Fig. 7. The horizontal axis is the *n* value at a wavelength of 450 nm.

The three observed σ_{ts}^{λ} values had very good correlations one another (Table 1). The estimated changes of σ_{ts}^{λ} due to a difference of 0.01 in the *n* value were approximately equal to standard errors derived from the observed σ_{ts}^{λ} values. The errors in the appropriate *n* values estimated below would be less than ± 0.01.

358 Fig. 7a shows the *p* values when the *n* value is constant, independent of the wavelength
359 of light. Even for the same material, the *n* value generally depends on the wavelength of
360 light and increases with decreasing wavelength. The *p* values for this case are shown in Fig.
361 7b. The mutual difference in *n* values among the three wavelengths was assumed to be
362 0.01 due to the normal dispersion. Fig. 7c shows the *p* values when the *n* value at 450 nm
363 is 0.01 higher than that at 550 and 700 nm. The case of anomalous dispersion, in which *n*
364 values decrease with decreasing wavelength, is shown in Fig. 7d. The *n* values at 450 nm
365 were assumed to be 0.02 lower than at 700 nm. In all cases, the *n* values were assumed to
366 be uniform from D_1 to the midpoint between D_8 and D_9 (Fig. 6). The minimum *p* value is
367 shown in Fig. 7d.

368 The effect of the light-absorbing component was not considered to reproduce the σ_{ts}^{λ}
369 values at each wavelength. In the number size distribution under *sf* = 0.475, with the particle
370 sizing of *m* (1.56, 0) in Fig. 7b, the *p* value was 2.84×10^{-3} in the assumption of the normal
371 dispersion. If the *k* value was uniform for particles with $D < D_6 = 1.17$ μm, as corrected by *m*
372 (1.56, 0.0168) (Table 2), the σ_{ts}^{λ} and σ_a values estimated at *sf* = 0.475 and *df* = 0.603 were
373 approximately equal to the observed values (Tables 1 and 3). The *p* value in the case of the
374 normal dispersion was minimal at 3.34×10^{-3}, compared with the other cases with *k*–value
375 assumptions in Figs. 7a, 7c, and 7d.

376 The column model in Fig. 8a consists of black solid and red dashed lines under *sf* =
377 0.475 with particle sizing for *m* (1.55, 0). The green solid and dashed curves are the

regression curves obtained by fitting the log-normal models for the column models that exclude and include the red dashed line, respectively. The number concentrations for m (1.53–1.57, 0) were within the range of the standard deviation of its averaged number concentrations (1.55, 0). Therefore, the green solid and dashed curves were used to estimate σ_{ts}^{λ} and σ_a values at wavelengths of 450, 550, and 700 nm without considering the wavelength dependence of particle sizing for m (n, k). Using Eqs. (3) and (4), and the assumption of the normal dispersion for the green solid and dashed curves, the estimated σ_{ts}^{λ} and σ_a values were almost identical to the observed values, although the k values were higher than those in the column model (Tables 1, 2, and 3). The estimated σ_a values were highest when $0.2 < D < 0.5$ μm (Fig. 9a). The number size distribution of particles with $D <$ 0.2 μm was different among the models (Fig. 8a). Consequently, the k value increased with decreasing number concentration of particles with D around 0.2 μm (Table 2).

4.2. Complex refractive indices of aerosol particles in pristine air masses

The observed σ_{ts}^{λ} and oAE_i from 17.5°N to 16.0°N are listed in Table 1. The oAE_i values showed the relationship $0 < oAE_1 < oAE_2 < oAE_3$. The σ_{ts}^{λ} values at each wavelength were estimated using Eqs. (2) and (4). Assuming that the n value was uniform from D_1 to the midpoint between D_8 and D_9 in the column model (Fig. 6), the values of eAE_i were always estimated to be < 0 independent of the n value. This result differed from that for oAE_i.

In general, the number size distributions have an inflection point at around 1 μm in diameter. The refractive index n_{1-6} values for particles from D_1 to D_6 may be different from the n_{6-9} values for particles from D_6 to D_9. Therefore, eAE_i values were calculated for combinations of different values in n_{1-6} and n_{6-9} at 0.05 intervals of 1.35 to 1.65. Two cases, $n_{1-6} > n_{6-9}$ and $n_{1-6} < n_{6-9}$, were considered in the estimation of the eAE_i values. No light-absorbing component, that is, $k = 0$, was assumed to simplify the determination of n value combinations.

In the case of $n_{1-6} > n_{6-9}$, the eAE_i values were estimated to be < 0 using n_{1-6} in particles with $D < D_6$ corrected by n_{1-6}, or $eAE_1 > eAE_2 > eAE_3$ using n_{1-6} in particles with $D < D_6$ corrected by n_{6-9}. These results differed from the relationship among oAE_i.

In the case of $n_{1-6} < n_{6-9}$, the eAE_i values were always estimated to be $eAE_1 < eAE_2 < eAE_3$, except for $n_{1-6} = 1.35$. The p values were always small when using n_{1-6} in particles with $D < D_6$ corrected by n_{6-9}, in comparison with using n_{1-6} in particles with $D < D_6$ corrected by n_{1-6}. The appropriate combinations of (n_{1-6}, n_{6-9}) were (1.45, 1.60) and (1.50, 1.65). Furthermore, p values in the ranges of n_{1-6} = 1.45–1.50 and n_{6-9} = 1.60–1.65 were calculated at intervals of 0.01 to determine the most suitable combination of n_{1-6} and n_{6-9}. The p value was minimal in the case of D_6 = 0.981 μm corrected by n_{6-9} = 1.62. By considering the k value in particles with $D < D_6$, the final appropriate values of n_{1-6}, n_{6-9}, and k were estimated to be 1.47, 1.62, and 0.0030, respectively, at all three wavelengths (Table 2). The normal dispersion did not contribute to the convergence of p values. The estimated

417 σ_{ts}^{λ} and σ_a values were the same as the observed values (Tables 1 and 3). In this case, *sf*

418 and *df* were 2.75 and 0.884, respectively.

419 The observed σ_{ts}^{λ}, σ_a, and oAE_i from 14.5°N to 13.5°N are listed in Table 1. The values

420 of n_{1-6} = 1.47 and n_{6-9} = 1.62 for aerosol particles from 17.5°N to 16.0°N were applied to

421 reproduce the values of σ_{ts}^{λ} and σ_a from 14.5°N to 13.5°N. The values of *p* at other *n* values

422 were higher than the *p* value in (n_{1-6}, n_{6-9}) = (1.47, 1.62). The minimum *p* value was 6.50 ×

423 10^{-6} in *k* = 0 and *sf* = 2.5. However, D_6 must be 1.038 μm (Fig. 10). The *p* value was sensitive

424 to the position of D_6 because *n* values differ across D_6. Assuming that the *k* value was 0.0055

425 for particles with $D < D_6$ (Table 2) and *df* of 0.828, the observed σ_{ts}^{λ} and σ_a values were

426 successfully reproduced by the column model (Tables 1 and 3).

427 The observed σ_{ts}^{λ} and σ_a values from 17.5°N to 16.0°N and from 14.5°N to 13.5°N were

428 also reproduced using the green solid and dashed curves obtained by fitting the log-normal

429 models for the column models (Figs. 8b and 8c). The σ_{ts}^{λ} and σ_a values estimated using

430 Eqs. (3) and (4) were almost the same as the observed values (Tables 1 and 3). The σ_{ts}^{λ}

431 values from 2 to 3 μm were slightly higher from 14.5°N to 13.5°N than 17.5°N to 16.0°N

432 (Figs. 9b and 9c). In the column model, the values of σ_a were zero for coarse particles. In

433 the log-normal model, however, the estimated σ_a values were in a comparatively wide size

434 range. Therefore, the *k* values in the log-normal model were lower than those in the column

435 model (Table 2).

436

5. Discussion

5.1. Polluted air masses

At a wavelength of 589 nm, the complex refractive indices are *m* (1.521, 0) for $(NH_4)_2SO_4$ and *m* (1.544, 0) for NaCl (Seinfeld and Pandis, 1998). The estimated *n* = 1.55 at a wavelength of 550 nm was close to these *n* values. Non-sea salt sulfates and sea salt are the primary chemical species in fine and coarse particles, respectively (Matsumoto et al., 1998; Campuzano-Jost et al., 2003; Heintzenberg et al., 2003).

Pollutants in the winter season are associated with black carbon from domestic coal burning (Dehkhoda et al., 2020). Using the shipboard measurements, Shiobara et al. (2007) estimated *m* (1.52−1.59, 0.002) in polluted air masses from the Asian continent over the western regions of the Ryukyu Islands of Japan. In the present study, the estimated *n* = 1.55 was within the range of Shiobara et al. (2007). Yabuki et al. (2003) estimated a maximum of *k* = 0.0114 in anthropogenic aerosols from 33.5°N to 30°N over the western North Pacific. Using sun photometer measurements, Bi et al. (2016) estimated *n* = 1.521 ± 0.025 and *k* = 0.00364 ± 0.0014 at a wavelength of 550 nm in the transported anthropogenic dust over East Asia. They also estimated that the refractive index at wavelengths ranging from 440 to 675 nm increased with an increase in wavelength. However, this was inconsistent with the normal dispersion estimated in the present study. Notably, these results are averages of aerosol optical properties from the surface to the top of the atmosphere. The *k* values

456 estimated in the present study were larger than those reported in previous studies due to
457 differences in size distribution assumptions for light–absorbing components (Table 2).
458
459 *5.2. Pristine air masses*
460 The complex refractive indices at 589 nm for NH_4HSO_4 and H_2SO_4 are *m* (1.473, 0) and
461 *m* (1.426, 0), respectively (Seinfeld and Pandis, 1998). The estimated *n* value for fine
462 particles was close to the real part of *m* (*n*, *k*) for NH_4HSO_4. Shiobara et al. (2007) estimated
463 *m* (1.38−1.40, < 0.001) in pristine air masses from the central North Pacific. Yabuki et al.
464 (2003) estimated *m* (1.35−1.37, < 0.0014) in marine aerosols from 28°N to 3°N. In the
465 present study, the estimated *n* and *k* values were higher than those reported by Shiobara et
466 al. (2007) and Yabuki et al. (2003). This is because they did not consider the size
467 dependence of *m* (*n*, *k*) when estimating the scattering and absorption coefficients. Virkkula
468 et al. (2006) found that the *n* value increased with increasing particle diameter in the
469 atmospheric boundary layer at the Finnish Antarctic Research Station. In the present study,
470 the value of *n* = 1.47 estimated for fine particles was close to that estimated by Virkkula et
471 al. (2006), while *n* = 1.62 for coarse particles was even higher than *n* = 1.544 for NaCl as
472 the primary chemical species. This suggests that coarse particles are composed of sea salt
473 and materials with *n* > 1.544. Water vapor was excluded as a candidate because *m* (1.333,
474 0) (Seinfeld and Pandis, 1998).

475 The uptake and volatilization rates of gas-phase species by aerosol particles depend
476 on the aerosol surface area per unit volume of air (Jacob, 2000). In the VOC-removed air
477 samples on Chichi-jima, the total surface area of the particles was smaller in August 2014
478 than in February 2015 (Fig. 5). However, in August 2014, the surface area with D > 1.1 μm
479 was approximately 3 times greater than that of 0.3 < D < 1.1 μm. The surface area of the
480 pre-existing particles in the VOC-removed air samples was maximum at approximately D =
481 3 μm. In addition, the effective diffusion rates for biogenic secondary organic materials
482 (SOM) were at least 1000 times greater than those of anthropogenic SOM (Liu et al., 2016).
483 Thus, VOCs appear to preferentially condense onto coarse particles. In the VOC-removed
484 air sample from February 2015, the surface area of D > 1.1 μm was about 0.7 times smaller
485 than that of 0.3 < D < 1.1 μm. In addition, the atmospheric VOC mixing ratios likely
486 decreased due to low biological activity. For these reasons, the differences in the number
487 size distributions between VOC-removed and untreated air samples would be more
488 conspicuous in summer than in winter.
489
490 *5.3. VOCs onto coarse particles in pristine air masses*
491 Colomb et al. (2009) measured DMS, isoprene, carbonyls, and organohalogens over
492 the Southern Indian Ocean. DMS was the most abundant VOC, with a mixing ratio ranging
493 from 50 to 885 pptv. The simultaneous enhancement of DMS, methyl bromide,
494 dibromomethane, and methyl iodine was associated with high biological activity. They also

showed that isoprene, terpenes, acetone, and acetaldehyde were biologically produced in the ocean. According to Rinaldi et al. (2010), increased VOC emissions by marine biota during the warm season results in relatively high WSOC concentrations in aerosol particles. Thus, atmospheric VOC mixing ratios are likely to be substantially higher in summer than in winter. This suggests that the volume of VOCs condensed on individual particles is larger in summer than in winter.

Most SOA masses consist of oligomeric compounds produced through gas-phase reactions between organic compounds and oxidants, such as O_3, OH, and NO_X (Denkenberger et al., 2007; Heaton et al., 2007). Kim et al. (2012) performed chamber experiments to investigate the refractive indices of SOA generated from the photooxidation of limonene and α–pinene with different HC/NOx ratios (ppbC ppb^{-1}). At a wavelength of 532 nm ranging from 1.34 to 1.56 for limonene and from 1.36 to 1.52 for α–pinene, the refractive indices increased with decreasing HC/NOx. Varma et al. (2013) reported the refractive indices for SOA from the reaction between β–pinene and NO_3. The refractive index was 1.61 ± 0.03 at wavelengths of 655−687 nm, under the condition of approximately 2 ppbC ppb^{-1}, which was lower than the lower limit of the experimental conditions in Kim et al. (2012). The results of Kim et al. (2012) and Varma et al. (2013) suggest that high refractive indices are associated with either a high proportion of organic nitrates or the possibility of oligomerization in SOA. The increase in H:C ratios was measured in the SOA formed by the photooxidation of limonene and α–pinene; as the particles grow, and the oxidation

515 progresses. The H:C ratio showed the best correlation with the refractive index. These
516 results are consistent with oligomerization reactions (Kim et al., 2014). Hall and Johnston
517 (2012) obtained MS/MS product ion spectra for many oligomers in SOAs produced by α–
518 pinene ozonolysis. They reported that a gas-phase monomer collided with the particle
519 surface and rapidly formed an oligomer.

520 Over the northwestern Pacific, WSOC mass concentrations were higher in coarse
521 particles than in fine particles under marine background conditions (Matsumoto et al., 1998;
522 Miyazaki et al., 2010). VOCs incorporated into aerosol particles could produce WSOC
523 through oxidation processes. The considerably high refractive index of coarse particles in
524 pristine air masses appears to be associated with the optical properties of VOCs and/or
525 SOAs condensed onto coarse particles.

6. Summary and conclusions

Scattering substances in aerosol particles disperse sunlight, whereas light-absorbing substances absorb sunlight. These optical properties depend on the *m* (*n*, *k*) of the materials contained in aerosol particles. In addition to the aerosol scattering and absorption coefficients, to elucidate the difference in the number size distribution between polluted and pristine air masses, the number size distributions of aerosol particles were measured on Chichi-jima of the Ogasawara Islands and the JARE52 voyage track of the icebreaker *Shirase* from Tokyo to the offing of the Philippines in the atmospheric boundary layer over the northwestern Pacific.

Scattering and absorption coefficients were reproduced from the observed number size distribution and the assumption of *m* (*n*, *k*). The following requirements were needed for the estimated values to be in harmony with the observed values: In polluted air masses from 30.5°N to 29.5°N, a refractive index of 1.55 for aerosol particles at a wavelength of 550 nm was estimated to be uniform regardless of the number size distribution, which was close to the values for $(NH_4)_2SO_4$ and NaCl. If $k = 0$ for coarse particles, the *k* values in the fine particles were 0.0168−0.0188. In addition, the refractive index, *n*, exhibits normal dispersion. In the pristine air masses from 17.5°N to 16.0°N and 14.5°N to 13.5°N, the refractive indices were estimated to be 1.47 for fine particles and 1.62 for coarse particles. The *k* values for fine particles were 0.0006−0.0030 from 17.5°N to 16.0°N and 0.0015−0.0055 from 14.5°N

to 13.5°N. The refractive index of the fine particles was close to that of NH_4HSO_4 while the refractive index of the coarse particles was even higher than the 1.544 of NaCl.

Based on the differences in number size distribution between the VOC-removed and untreated air samples observed on Chichi-jima, VOCs appear to preferentially condense onto coarse particles. Previous laboratory experiment studies have suggested that high refractive indices are associated with the oligomerization of SOA. The results of the present study indicate that the *m* (*n*, *k*) of coarse particles in real air masses was most likely affected by organic compounds originating from biological activity.

Coarse particles probably act as the sink for VOCs and/or SOA, and the reaction media of reactive species; they could also affect the production of cloud droplets, chemical lifetimes of reactive species, and radiative effects of aerosol particles. Therefore, in the marine atmosphere, further investigation should be conducted on the relationship between optical properties and organic compounds in coarse particles.

Data Availability Statement

The observational data used in this study are available in J-STAGE Data.

https://doi.org/10.34474/data.jmsj.xxxxxxx

Acknowledgements

I am indebted to M. Wada, M. Shiobara, and K. Hara for their valuable advice and thoughtful support. T. Kinase created and operated the sample-air heating system. This research focuses on the advanced preparation and operation of devices by T. Kinase and T. Murayama. I am grateful to M. Kawai for providing me with materials required to correct the PSAP values. I would also like to thank K. Matsumoto and F. Ito for their valuable comments. Special thanks to T. Yoshiyama of Tokyo–bika Co. Ltd. at the Ogasawara downrange station of the Japan aerospace exploration agency for his assistance with observations. I wish to express my gratitude to Bernhard Michel for providing the MieCalc software. This study was part of the Science Program of the Japanese Antarctic Research Expedition (JARE) and was supported by the National Institute of Polar Research (NIPR) under MEXT (Grant number AP11, Chief scientist, M. Hayashi). It was also supported by the NIPR through General Collaboration Project No. 2–16. I would like to thank Editage (www.editage.com) for their assistance with English language editing.

580 **References**

581

582 Anderson, T.L. and J.A. Ogren, 1998: Determining aerosol radiative properties using the
583 TSI 3563 integrating nephelometer. *Aerosol Sci. Technol*., **29**, 57–69.
584 Bates, T.S., J.A. Calhoun, and P.K. Quinn, 1992: Variations in the methanesulfonate to
585 sulfate molar ratio in submicrometer marine aerosol particles over the south Pacific
586 Ocean. *J. Geophys. Res*.: *Atmos*., **97**, 9859–9865.
587 Bi, J., J. Huang, B. Holben, and G. Zhang, 2016: Comparison of key absorption and
588 optical properties between pure and transported anthropogenic dust over East and
589 Central Asia. *Atmos. Chem. Phys*., **16**, 15501–15516.
590 Bikkina, S., K. Kawamura, Y. Miyazaki, and P. Fu, 2014: High abundances of oxalic,
591 azelaic, and glyoxylic acids and methylgyoxal in the open ocean with high biological
592 activity: Implication for secondary OA formation from isoprene. *Geophys. Res. Lett*., **41**,
593 3649–3657.
594 Bohren, C.F. and D.R. Huffman, 1998: *Absorption and scattering of light by small particles*.
595 John Wiley & Sons, New York, USA, p.27.
596 Bond, T.C., T.L. Anderson, and D. Campbell, 1999: Calibration and intercomparison of
597 filter–based measurements of visible light absorption by aerosols. *Aerosol Sci. Technol.*,
598 **30**, 582–600.

599 Bond, T.C. and R.W. Bergstrom, 2006: Light absorption by carbonaceous particles: An
600 investigative review. *Aerosol Sci. Technol*., **40**, 27–67.
601 Bond T.C., S.J. Doherty, D.W. Fahey, P.M. Forster, T. Berntsen, B.J. DeAngelo, M.G.
602 Flanner, S. Ghan, B. Kärcher, D. Koch, S. Kinne, Y. Kondo, P.K. Quinn, M.C. Sarofim,
603 M.G. Schultz, M. Schulz, C. Venkataraman, H. Zhang, S. Zhang, N. Bellouin, S.K.
604 Guttikunda, P.K. Hopke, M.Z. Jacobson, J.W. Kaiser, Z. Klimont, U. Lohmann,J. P.
605 Schwarz, D. Shindell, T. Storelvmo, S.G. Warren, and C.S. Zender, 2013: Bounding the
606 role of black carbon in the climate system: A scientific assessment. *J. Geophys. Res*.:
607 *Atmos*., **118**, 5380–5552.
608 Campuzano-Jost, P., C.D. Clark, H. Marring, D.S. Covert, S. Howell, V. Kapustin, K.A.
609 Clarke, E.S. Saltzman, and A.J. Hynes, 2003: Near–real–time measurement of sea–salt
610 aerosol during the SEAS campaign: Comparison of emission-based sodium detection
611 with an aerosol volatility technique. *J. Atmos. Oceanic Technol*., **20**, 1421–1430.
612 Ceburnis, D., C.D. O'Dowd, G.S. Jennings, M.C. Facchini, L. Emblico, S. Decesari, S.
613 Fuzzi, and J. Sakalys, 2008: Marine aerosol chemistry gradients: Elucidating primary
614 and secondary processes and fluxes. *Geophys. Res. Lett*., **35**, L07804,
615 doi:10.1029/2008GL033462.
616 Clarke, A.D., Y. Shinozuka, V.N. Kapustin, S. Howell, B. Huebert, S. Doherty, T.
617 Anderson, D. Covert, J. Anderson, X. Hua, K.G. Moore II, C. McNaughton, G.
618 Carmichael, and R. Weber, 2004: Size distributions and mixtures of dust and black

carbon aerosol in Asian outflow: physiochemistry and optical properties. *J. Geophys. Res.*: *Atmos.*, **109**, D15S09, doi:10.1029/2003JD004378.

Colomb, A., V. Gros, S. Alvain, R. Sarda-Esteve, B. Bonsang, C. Moulin, T. Klüpfel, and J. Williams, 2009: Variation of atmospheric volatile organic compounds over the Southern Indian Ocean (30-49°S). *Environ. Chem.*, **6**, 70–82.

Dall'Osto, M., D. Ceburnis, C. Monahan, D. R. Worsnop, J. Bialek, M. Kulmala, T. Kurtén, M. Ehn, J. Wenger, J. Sodeau, R. Healy, and C. O'Dowd, 2012: Nitrogenated and aliphatic organic vapors as possible drivers for marine secondary organic aerosol growth. *J. Geophys. Res.*, **117**, D12311, doi:10.1029/2012JD017522.

Decesari, S., E. Finessi, M. Rinaldi, M. Paglione, S. Fuzzi, E.G. Stephanou, T. Tziaras, A. Spyros, D. Ceburnis, C. O'Dowd, M. Dall'Osto, R.M. Harrison, J. Allan, H. Coe, and M.C. Facchini, 2011: Primary and secondary marine organic aerosols over the North Atlantic Ocean during the MAP experiment. *J. Geophys. Res.*, **116**, D22210, doi:10.1029/2011JD016204.

Dehkhoda, N., Y. Noh, and S. Joo, 2020: Long–term variation of black carbon absorption aerosol optical depth from AERONET data over East Asia. *Remote Sens.*, **12**, 21, 3551, doi:10.3390/rs12213551.

Denkenberger, K., R.C. Moffet, J.C. Holecek, T. P. Rebotier, and K.A. Prather, 2007: Real-time, single–particle measurements of oligomers in aged ambient aerosol particles. *Environ. Sci. Technol.*, **41**, 5439–5446.

639 Facchini, M.C, S. Decesari, M. Rinaldi, C. Carbone, E. Finessi, M. Mircea, S. Fuzzi, F.
640 Moretti, E. Tagliavini, D. Ceburnis, and C.D. O'Dowd, 2008: Important source of marine
641 secondary organic aerosol from biogenic amines. *Environ. Sci. Technol*., **42**, 9116–
642 9121.
643 Gantt, B., N. Meskhidze, and D. Kamykowski, 2009: A new physically–based quantification
644 of marine isoprene and primary organic aerosol emissions. *Atmos. Chem. Phys*., **9**,
645 4915–4927.
646 Hall, W. and M.V. Johnston, 2012: Oligomer formation pathways in secondary organic
647 aerosol from MS and MS/MS measurements with high mass accuracy and resolving
648 power. *J. Am. Soc. Mass Spectrom.*, **23**, 1097–1108.
649 Heaton, K.J., M.A. Dreyfus, S. Wang, and M.V. Johnston, 2007: Oligomers in the early
650 stage of biogenic secondary organic aerosol formation and growth. *Environ. Sci.*
651 *Technol.*, **41**, 6129–6136.
652 Heintzenberg, J., F. Raes, and S.E. Schwartz (Lead authors), 2003: Tropospheric
653 aerosols. *Atmospheric chemistry in a changing world*. Brasseur, G.P. et al. (eds.),
654 Springer-Verlag, Berlin, Germany, 125–156 pp.
655 Hinds, W.C., 1999: *Aerosol Technology: Properties, behavior, and measurement of*
656 *airborne particles*. John Wiley & Sons, New York, USA, 8 and 353 pp.
657 Hodkinson, J.R. and J.R. Greenfield, 1965: Response calculations for light-scattering
658 aerosol counters and photometers. *Appl. Opt*., **4**, 1463–1474.

659 IPCC, 2013: The Physical science basis. Contribution of working group I to the fifth
660 assessment report of the intergovernmental panel on climate change, *Climate Change*
661 *2013* [Stocker, T.F., D. Qin, G.-K. Plattner, M. Tignor, S.K. Allen, J. Boschung, A.
662 Nauels, Y. Xia, V. Bex, and P.M. Midgley (eds.)]. Cambridge University Press,
663 Cambridge, United Kingdom and New York, USA, p.1535.
664 Jacob, D.J., 2000: Heterogeneous chemistry and tropospheric ozone. *Atmos. Environ*., **34**,
665 2131–2159.
666 Jaenicke, R., 1993: Tropospheric aerosols. *Aerosol–Cloud–Climate Interactions*. P.V.
667 Hobbs P.V. (ed.), Academic Press, San Diego, CA., 1–31 pp.
668 Kim, H., B. Barkey, and S.E. Paulson, 2012: Real refractive indices and formation yields of
669 secondary organic aerosol generated from photooxidation of limonene and α–pinene:
670 The effect of the HC/NOx ratio. *J. Phys. Chem*., **116**, 6059–6067.
671 Kim, H., S. Liu, L.M. Russell, and S.E. Paulson, 2014: Dependence of real refractive
672 indices on O:C, H:C and mass fragments of secondary organic aerosol generated from
673 ozonolysis and photooxidation of limonene and α–pinene. *Aerosol Sci. Technol.,* **48**,
674 498–507.
675 Koga, S. and H. Tanaka, 1999: Modeling the methanesulfonate to non-sea-salt sulfate
676 molar ratio and dimethylsulfide oxidation in the atmosphere. *J. Geophys. Res*., **104**,
677 13735–13747.

678 Koga, S., T. Maeda, and N. Kaneyasu, 2008: Source distributions to black carbon mass
679 fractions in aerosol particles over the northwestern Pacific. *Atmos. Environ*., **42**, 800–
680 814.
681 Koga, S., 2021: Optical properties of aerosol particles in the atmospheric boundary layer in
682 regions with and without sea ice. *Polar Sci*., **29**, 100704,
683 doi:10.1016/j.polar.2021.100704.
684 Kulmala, M., H. Vehkamäki, T. Petäjä, M. Dal Maso, A. Lauri, V.-M. Kerminen, W. Birmili,
685 and P.H. McMurry, 2004: Formation and growth rates of ultrafine atmospheric particles:
686 a review of observations. *J. Aerosol Sci*., **35**, 143–176.
687 Liu, P., Y.J. Li, Y. Wang, M.K. Gilles, R.A. Zaveri, A.K. Bertram, and S.T. Martin, 2016:
688 Lability of secondary organic particulate matter. *Proc. Natl. Acad. Sci. U. S. A.*, **113**,
689 12643–12648.
690 Mahajan, A.S., S. Fadnavis, M.A. Thomas, L. Pozzoli, S. Gupta, S.J. Royer, A. Saiz-
691 Lopez, and R. Simó, 2015: Quantifying the impacts of an updated global dimethyl sulfide
692 climatology on cloud microphysics and aerosol radiative forcing. *J. Geophys. Res*.:
693 *Atmos*., **120**, 2524–2536.
694 Matsumoto, K., I. Nagao, H. Tanaka, H. Miyaji, T. Iida, T., and Y. Ikebe, 1998: Seasonal
695 characteristics of organic and inorganic species and their size distributions in
696 atmospheric aerosols over the northwest Pacific Ocean. *Atmos. Environ*., **32**, 1931–
697 1946.

698 Miyazaki, Y., K. Kawamura, and M. Sawano, 2010: Size distributions and chemical
699 characterization of water-soluble organic aerosols over the western North Pacific in
700 summer. *J. Geophys. Res.*: *Atmos.*, **115**, D23210, doi:10.1029/2010JD014439.
701 Novakov, T. and J.E. Penner, 1993: Large contribution of organic aerosols to cloud–
702 condensation–nuclei concentrations. *Nature*, **365**, 823–826.
703 O'Dowd, C.D., M.C. Facchini, F. Cavalli, D. Ceburnis, M. Mircea, S. Decesari, S. Fuzzi, Y.
704 J. Yoon, and J.-P. Putaud, 2004: Biogenically driven organic contribution to marine
705 aerosol. *Nature*, **431**, 676–680.
706 O'Dowd, C., C. Monahan, and M. Dall'Osto, 2010: On the occurrence of open ocean
707 particle production and growth events. *Geophys. Res. Lett.*, **37**, L19805,
708 doi:10.1029/2010GL044679.
709 Ohta, S., N. Murao, and S. Yamagata, 2013: Optical and chemical properties of
710 atmospheric aerosols at Amami Oshima and Fukue Islands in Japan in spring, 2001. *J.*
711 *Meteor. Soc. Jpn.*, **91**, 63–73.
712 Pirjola, L., C.D. O'Dowd, I.M. Brooks, and M. Kulmala, 2000: Can new particle formation
713 occur in the clean marine boundary layer? *J. Geophys. Res.*: *Atmos.*, **105**, 26531–
714 26546.
715 Read, K.A., A.C. Lewis, S. Bauguitte, A.M. Rankin, R.A. Salmon, E.W. Wolff, A. Saiz-
716 Lopez, W.J. Bloss, D.E. Heard, J.D. Lee, and J.M.C. Plane, 2008: DMS and MSA

717 measurements in the Antarctic boundary layer: Impact of BrO on MSA production.
718 *Atmos. Chem. Phys*., **8**, 2985–2997.
719 Rinaldi, M., S. Decesari, E. Finessi, L. Giulianelli, C. Carbone, S. Fuzzi, C.D. O'Dowd, D.
720 Ceburnis, and M.C. Facchini, 2010: Primary and secondary organic marine aerosol and
721 oceanic biological activity: Recent results and new perspectives for future studies. *Adv.*
722 *Meteor*., 1–10, doi:10.1155/2010/310682.
723 Rolph, G., A. Stein, and B. Stunder, 2017: Real-time Environmental Applications and
724 Display sYstem: READY. *Environ. Modell. Software*, **95**, 210–228.
725 Savoie, D.L. and J.M. Prospero, 1982: Particle size distribution of nitrate and sulphate in
726 the marine atmosphere. *Geophys. Res. Lett*., **9**, 1207–1210.
727 Seinfeld, J.H. and S.N. Pandis, 1998: *Atmospheric chemistry and physics*: *From air*
728 *pollution to climate change*, John Wiley & Sons, New York, 429, 1118, 1125, 1131, and
729 1134 pp.
730 Shaw, S.L., B. Gantt, and N. Meskhidze, 2010: Production and emissions of marine
731 isoprene monoterpenes: A review. *Adv. Meteor*., **2010**, 1–24, doi:10.1155/2010/408696.
732 Shiobara, M., K. Hara, M. Yabuki, and H. Kobayashi, 2007: Optical and chemical
733 properties of marine boundary–layer aerosol around Japan determined from shipboard
734 measurements in 2002. *Atmos. Environ*., **41**, 4638–4652.
735 Srivastava, A.K., B.J. Mehrotra, A. Singh, V. Singh, D.S. Bisht, S. Tiwari, and M.K.
736 Srivastava, 2020: Implications of different aerosol species to direct radiative forcing and

737 atmospheric heating rate. *Atmos. Environ.*, **241**, 117820,
738 doi:10.1016/j.atmosenv.2020.117820.
739 Stein, A.F., R.R. Draxler, G.D. Rolph, B.J.B. Stunder, M.D. Cohen, and F. Ngan, 2015:
740 NOAA's HYSPLIT atmospheric transport and dispersion modeling system. *Bull. Amer.*
741 *Meteor. Soc.*, **96**, 2059–2077.
742 Sullivan, P.D., B.R. Stone, Z. Hashisho, and M.J. Rood, 2007. Water adsorption with
743 hysteresis effect onto microporous activated carbon fabrics. *Adsorption*, **13**, 173–189.
744 Varma, R.M., S.M. Ball, T. Brauers, H.-P. Dorn, U. Heitmann, R.L. Jones, U. Platt, D.
745 Pöhler, A.A. Ruth, A.J.L. Shillings, J. Thieser, A. Wahner, and D.S. Venables, 2013.
746 Light extinction by secondary organic aerosol: an intercomparison of three broadband
747 cavity spectrometers. *Atmos. Meas. Tech.*, **6**, 3115–3130.
748 Virkkula, A., I.K. Koponen, K. Teinilä, R. Hillamo, V.-M. Kerminen, and M. Kulmala, 2006:
749 Effective real refractive index of dry aerosols in the Antarctic boundary layer. *Geophys.*
750 *Res. Lett.*, **33**, L06805, doi:10.1029/2005GL024602.
751 Weber, R.J., P.H. McMurry, R.L. Mauldin III, D.J. Tanner, F.L. Eisele, A.D. Clark, and V.N.
752 Kapustin, 1999: New particle formation in the remote troposphere: A comparison of
753 observations at various sites. *Geophys. Res. Lett.*, **26**, 307–310.
754 Yabuki, M., M. Shiobara, H. Kobayashi, M. Hayashi, K. Hara, K. Osada, H. Kuze, and N.
755 Takeuchi, 2003: Optical properties of aerosols in the marine boundary layer during a
756 cruise from Tokyo, Japan to Fremantle, Australia. *J. Meteor. Soc. Jpn.*, **81**, 151–162.

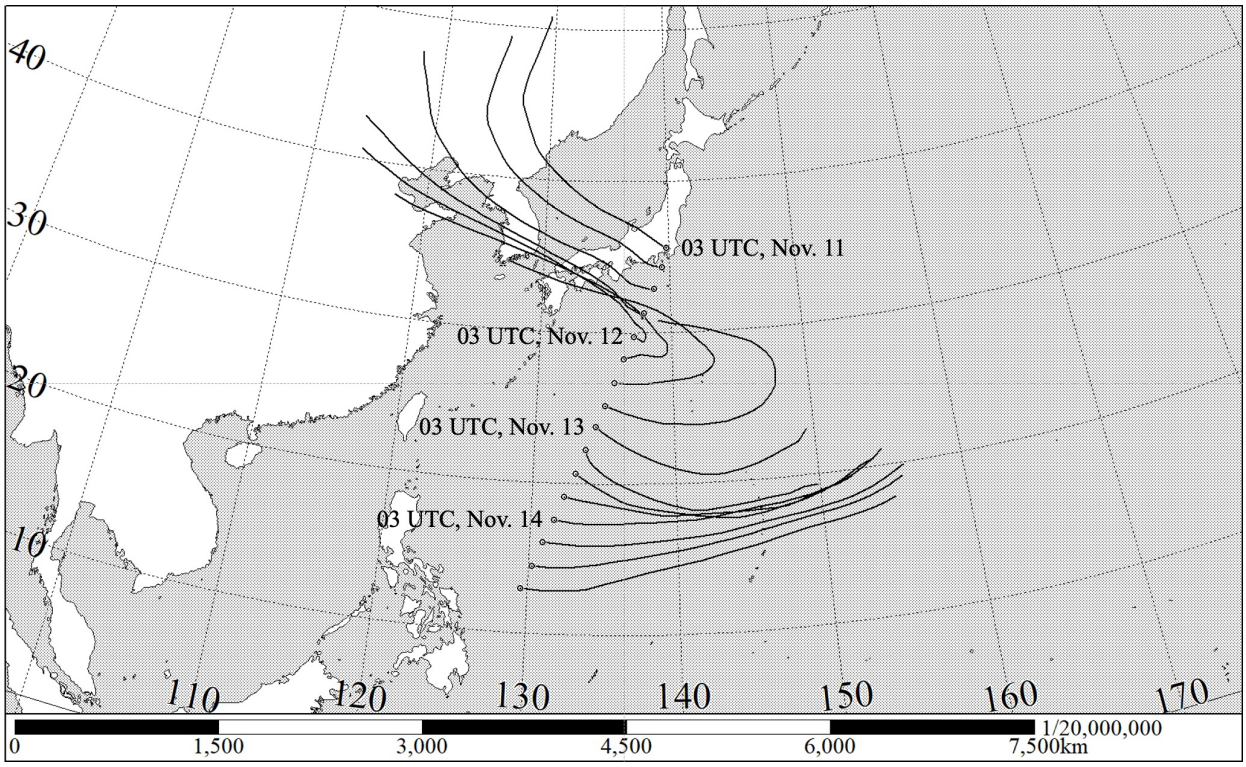

757

758 Fig. 1 The JARE52 voyage track of the icebreaker *Shirase* from Tokyo, Japan, to the offing

759 of the Philippines on November 11−14, 2010.

760

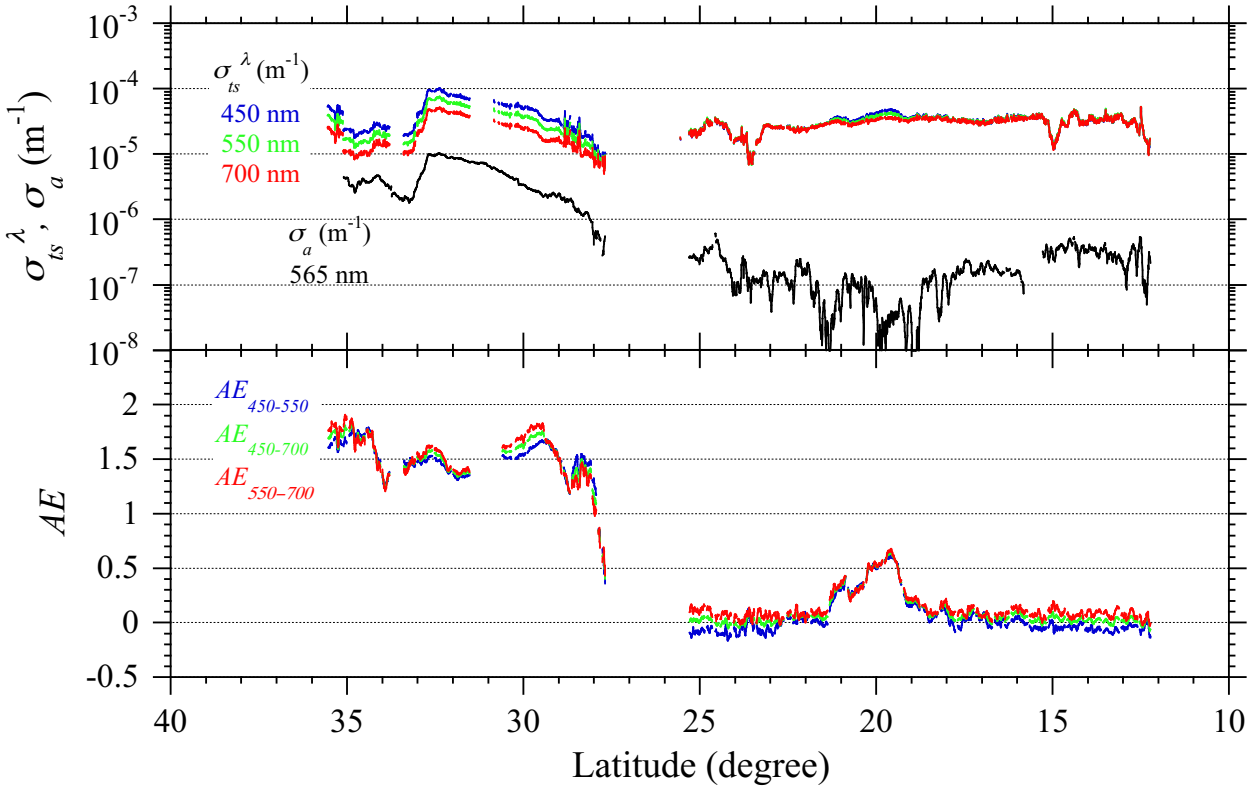

761

762 Fig. 2 Observed σ_{ts}^{λ} at wavelengths of 450, 550, and 700 nm, σ_a at 565 nm, and *AE* at

763 three wavelength ranges. The values of σ_{ts}^{λ} and σ_a are values at 1 min intervals. The

764 values of *AE* are 1 h moving averages.

765

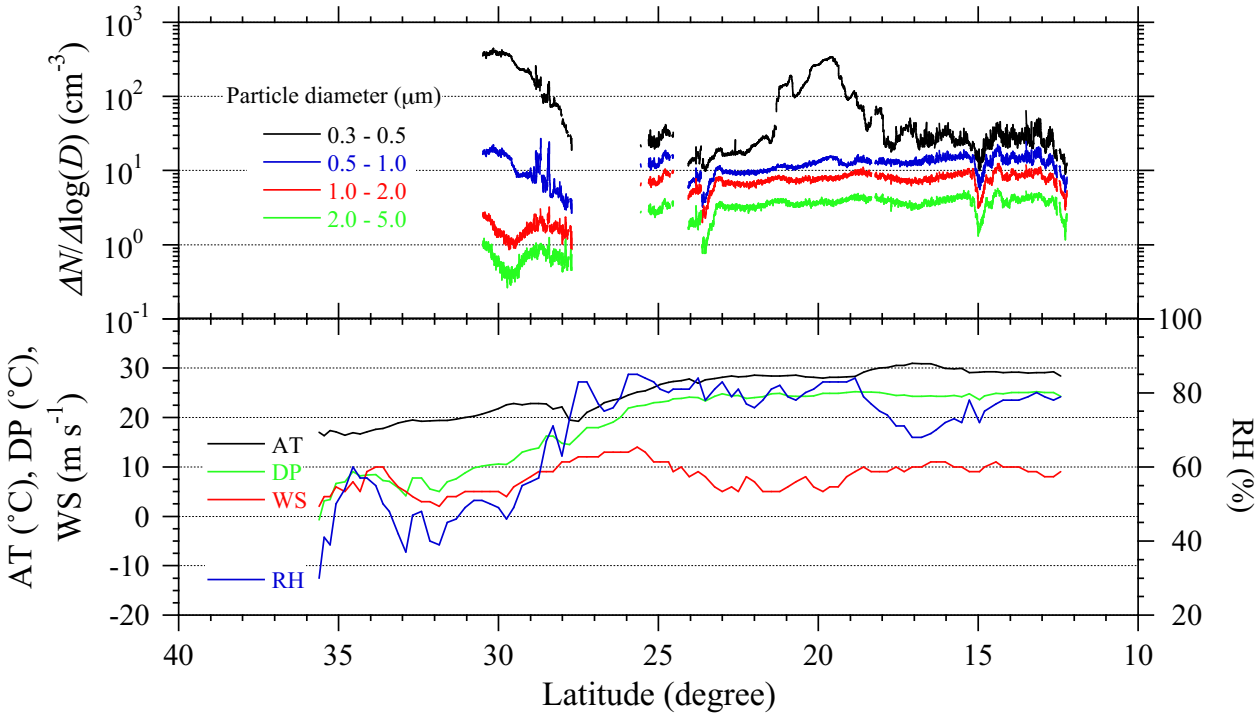

766

767 Fig. 3 Number size concentrations of 0.3−5.0 μm diameter aerosol particles at 1 min

768 intervals, and air temperature (AT), dew point (DP), wind speed (WS), and relative

769 humidity (%) at 1 h intervals.

770

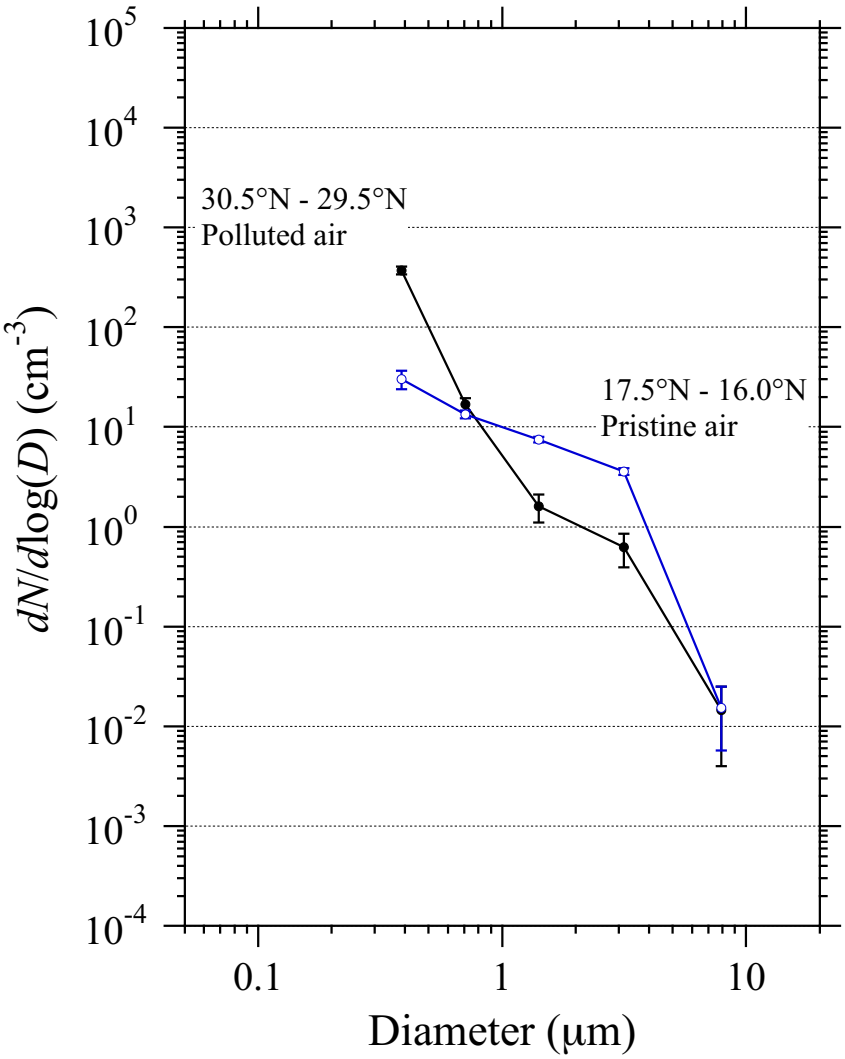

771

772 Fig. 4 Number size distributions averaged from 30.5°N to 29.5°N and from 17.5°N to

773 16.0°N in Fig. 3. Vertical bars represent the range of one standard deviation.

774

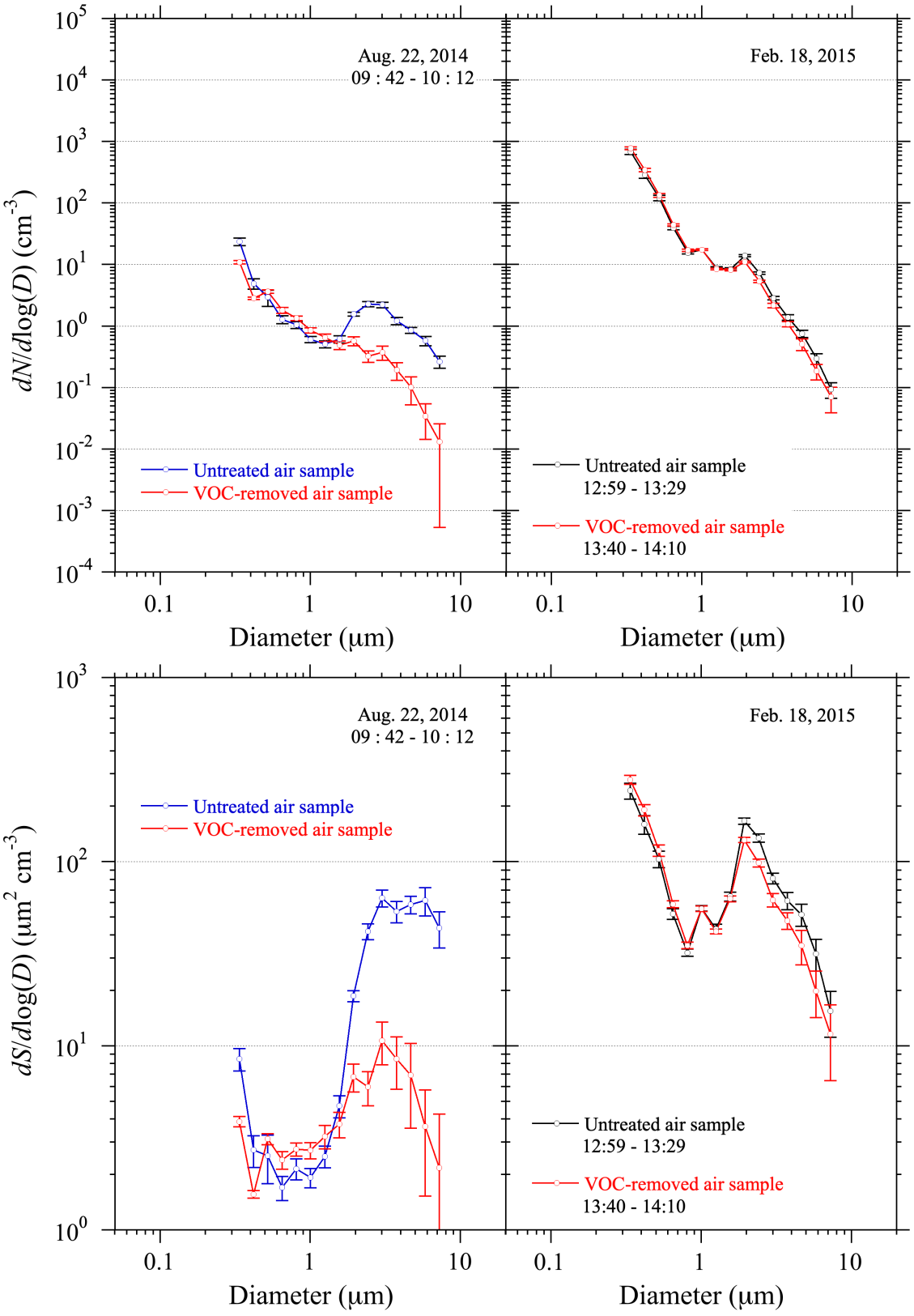

775

776 Fig. 5 Number and surface area size distributions measured on Chichi-jima, the

777 Ogasawara Islands, in the northwestern Pacific. Vertical bars represent the range of one

778 standard deviation.

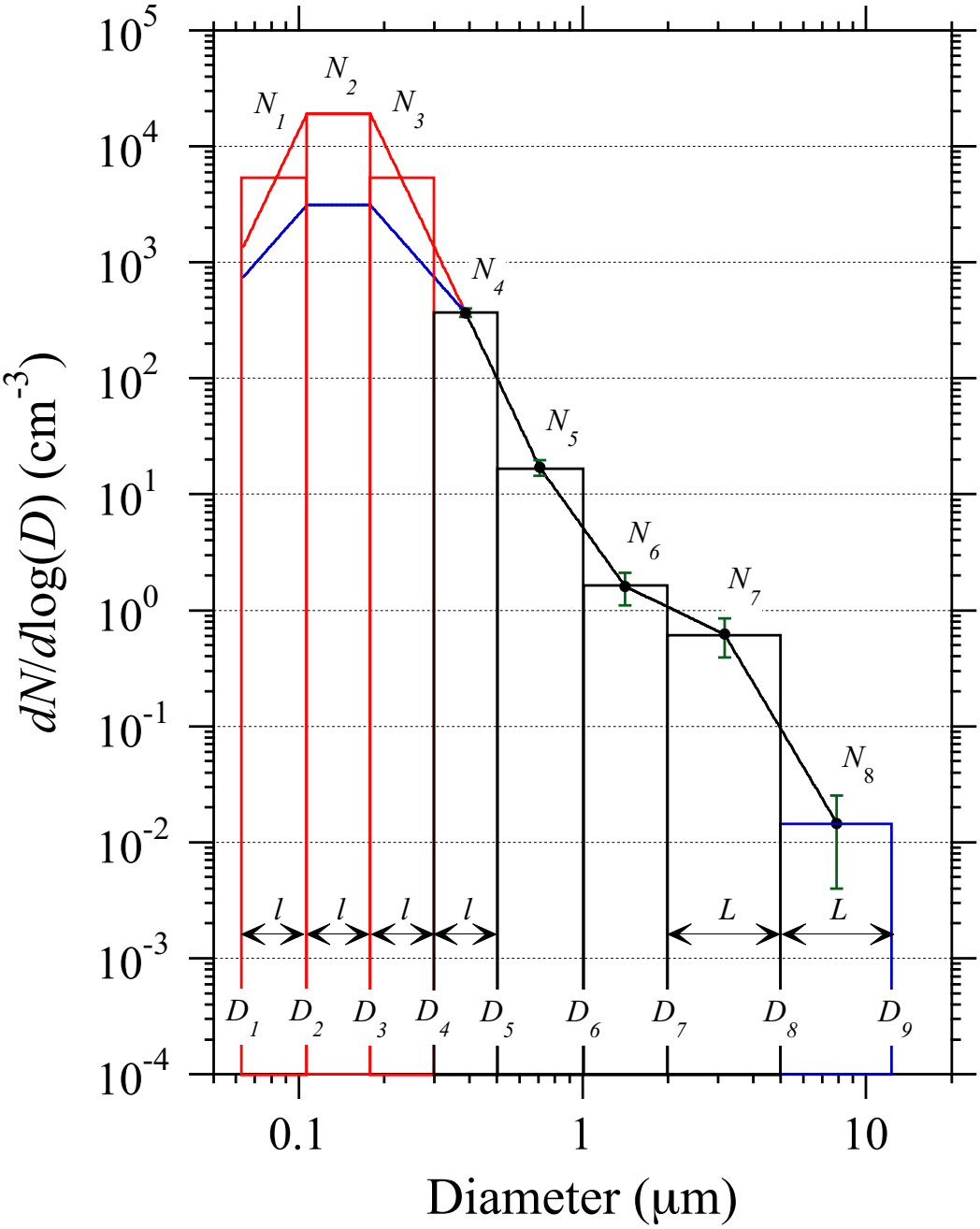

779

780 Fig. 6 Conceptual diagram of the column model. The black dots show the number size

781 distributions of aerosol particles reported by the OPC in polluted air masses from 30.5°N

782 to 29.5°N. Vertical bars represent the range of one standard deviation. For more

783 information, see text.

784

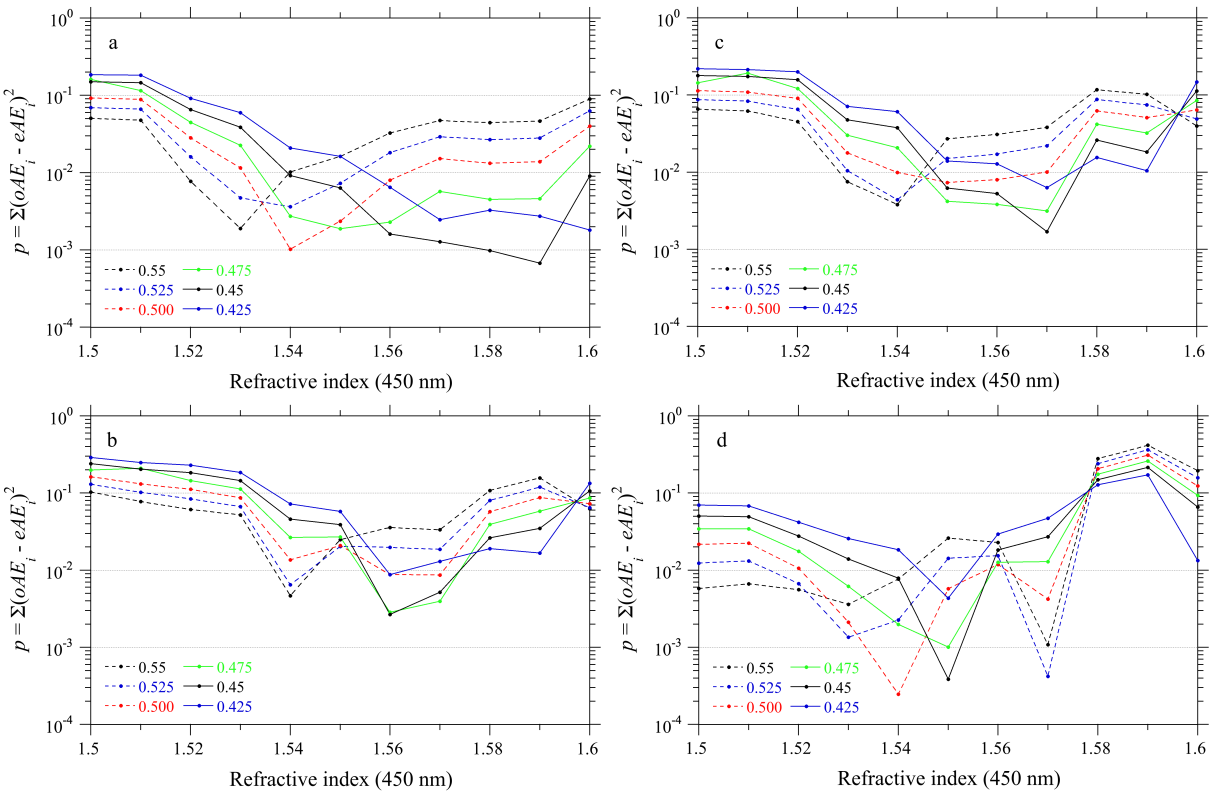

785

786 Fig. 7 Variations of the *p* value as a function of *m*(*n*, 0) at a wavelength of 450 nm. These

787 values are obtained by *sf* from 0.425 to 0.55 at intervals of 0.025. (a) The refractive

788 index is constant, independent of wavelength of light. (b) The mutual difference in the

789 refractive indices among the 450, 550, and 700 nm wavelengths is assumed to be 0.01

790 due to normal dispersion. (c) The refractive index at 450 nm is 0.01 higher than those at

791 550 and 700 nm. (d) The case, anomalous dispersion, that refractive index decreases

792 with decreasing the wavelength. The refractive index at 450 nm is assumed to be 0.02

793 lower than at 700 nm.

794

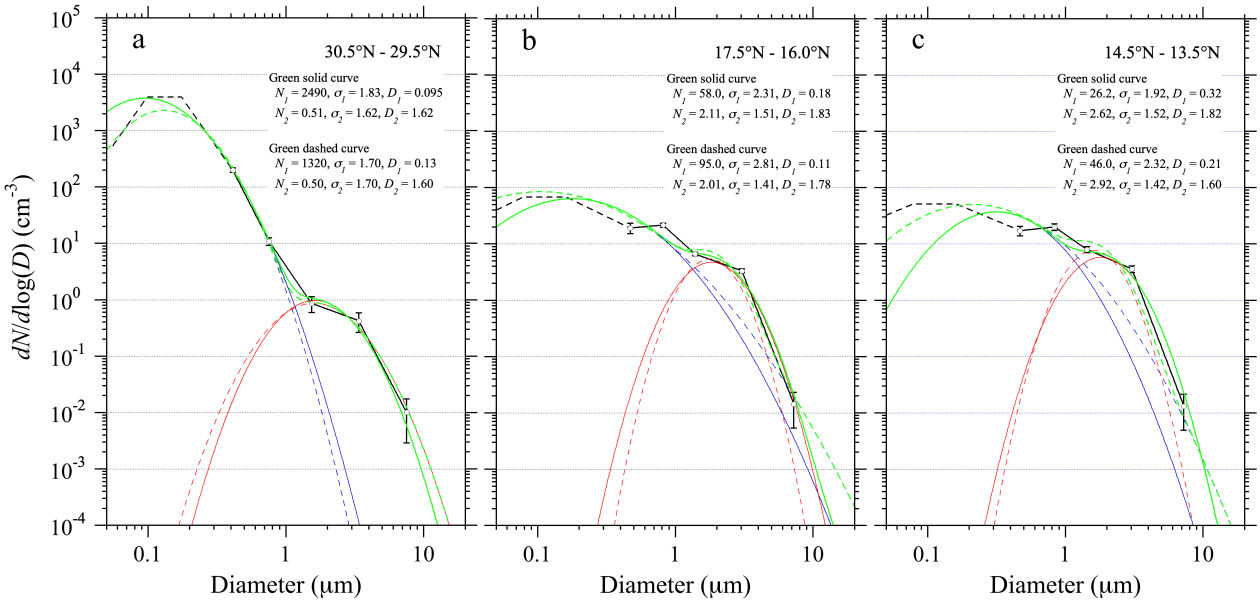

795

796 Fig. 8 Number size distributions in (a) polluted, and (b) and (c) pristine air masses. Open

797 circles show the arithmetic means with one standard deviations of the corrected number

798 size distributions. The black solid and red dashed lines are the expanded number size

799 distribution, as the column model. The green solid and dashed curves, as the log–

800 normal model, are composed of the blue and red solid curves, and the blue and red

801 dashed curves, respectively.

802

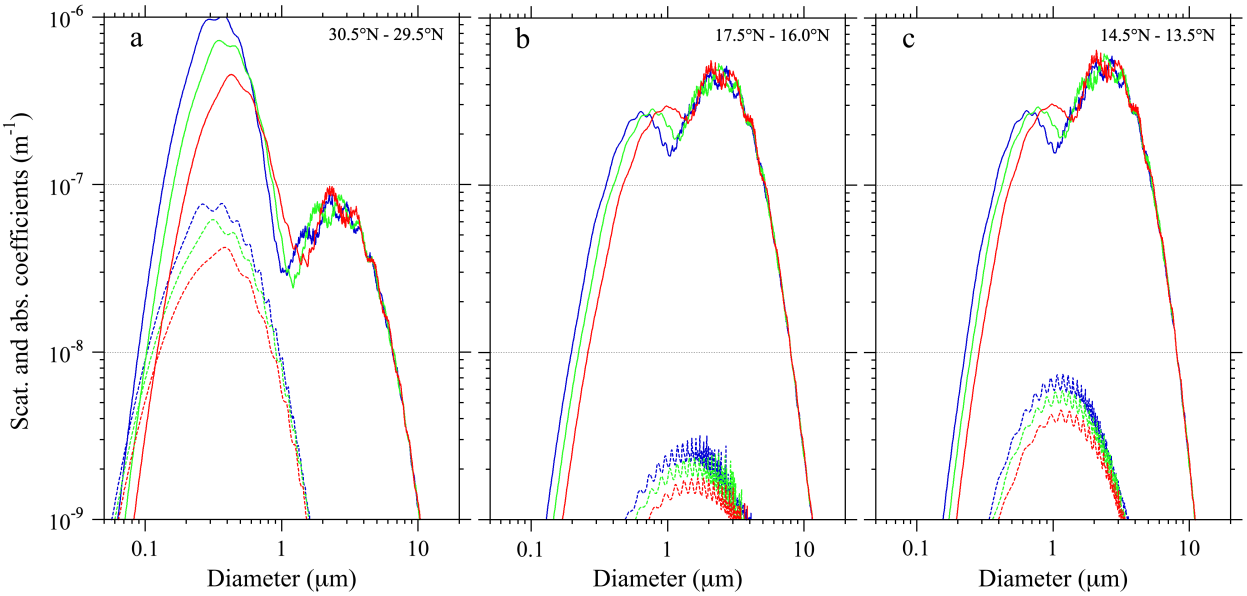

803

804 Fig. 9 Scattering and absorption coefficients at wavelengths of 450 nm (blue), 550 nm

805 (green), and 700 nm (red) as a function of particle diameter (a) from 30.5°N to 29.5°N,

806 (b) from 17.5°N to 16.0°N, and (c) from 14.5°N to 13.5°N. Dashed curves represent

807 absorption coefficients.

808

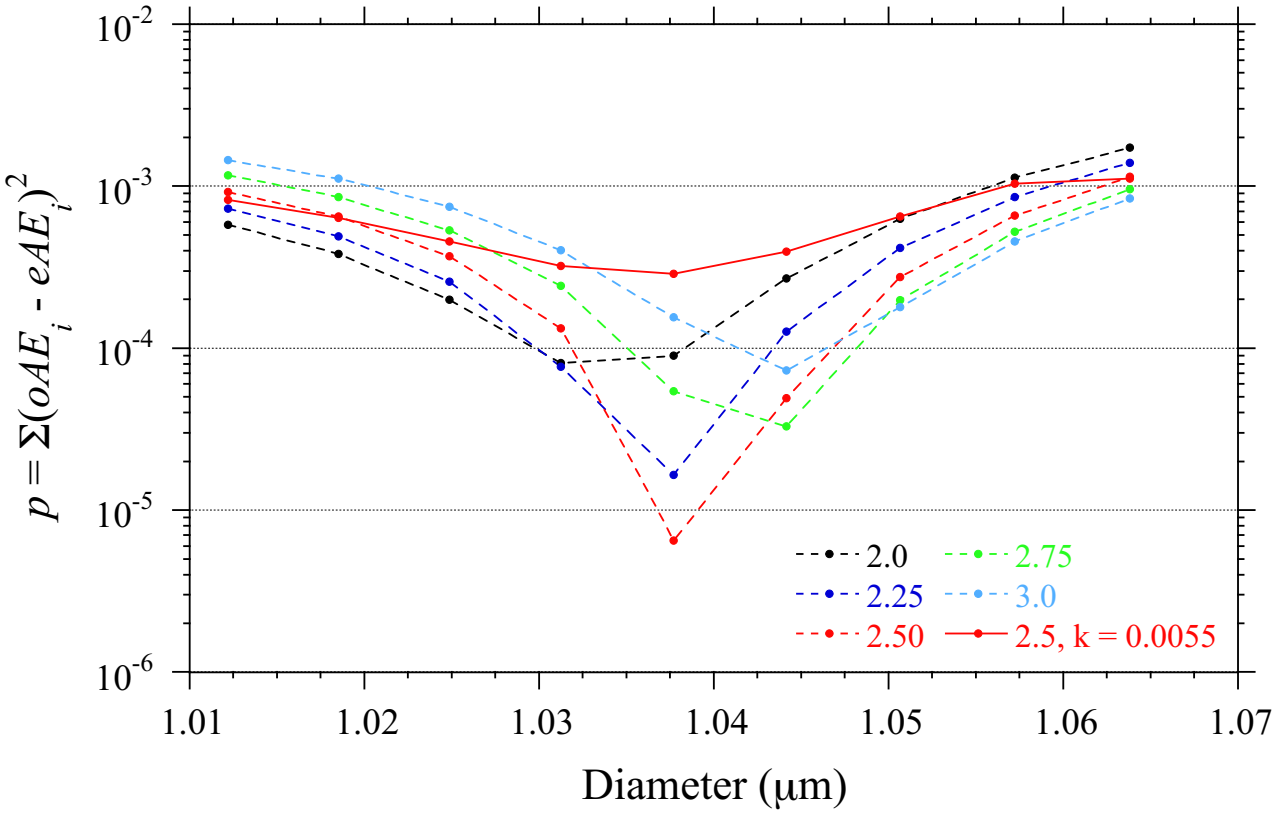

809

810 Fig.10 Variations of the *p* value as a function of particle diameter D_6 in the column model

811 from 14.5°N to 13.5°N. These values are obtained by *sf* from 2.0 to 3.0 at intervals of 0.25.

812 The red solid line shows the *p* values in *sf* = 2.5 and *k* = 0.0055.

813

814 Table 1 C^{λ}, $\sigma_{ts}{}^{\lambda}$ ($\times 10^{-6}$ m^{-1}), σ_a ($\times 10^{-6}$ m^{-1}), *SSA*, and *AE* averaged in polluted and

815 pristine air masses, and *r*.

	Wavelength nm	Polluted air	Pristine air	
		30.5°N - 29.5°N	17.5°N - 16.0°N	14.5°N - 13.5°N
C^{λ}	450	1.13 ± 0.01	1.38 ± 0.02	1.40 ± 0.02
	550	1.12 ± 0.01	1.35 ± 0.01	1.36 ± 0.01
	700	1.11 ± 0.01	1.30 ± 0.01	1.31 ± 0.01
$\sigma_{ts}{}^{\lambda}$	450	49.95 ± 4.95	32.52 ± 2.32	34.79 ± 4.69
	550	36.48 ± 3.94	32.38 ± 2.32	35.14 ± 4.71
	700	24.09 ± 2.91	31.70 ± 2.19	34.48 ± 4.67
σ_a	565	3.45 ± 0.71	0.175 ± 0.03	0.353 ± 0.06
SSA	550	0.914 ± 0.018	0.995 ± 0.001	0.990 ± 0.002
AE	450 - 550	1.57	0.02	- 0.05
	450 - 700	1.65	0.06	0.02
	550 - 700	1.72	0.09	0.08
r	450 - 550	0.997	0.98	0.995
	450 - 700	0.981	0.947	0.991
	550 - 700	0.989	0.966	0.992

816

817

818 Table 2 Estimated *m* (*n*, *k*) in polluted and pristine air masses.

Model	Wavelength nm	Polluted air 30.5°N - 29.5°N				Pristine air					
		n	*k*			*n*		*k*			
		Fine, Coarse	Fine		Coarse	Fine	Coarse	Fine			Coarse
								17.5°N - 16.0°N		14.5°N - 13.5°N	
Column	450	1.56									
	550	1.55	0.0168		0	1.47	1.62	0.0030		0.0055	0
	700	1.54									
			GSC[a]	GDC[a]				GSC[b]	GDC[b]	GSC[c]	GDC[c]	
log-normal	450	1.56										
	550	1.55	0.0178	0.0188	0*	1.47	1.62	0.0010	0.0006	0.0030	0.0015	0*
	700	1.54										

819

820 GSC and GDC are acronyms of green solid curve and green dashed curve in Fig. 8,
821 respectively. a, b, and c represent curves in Figs. 8a, 8b, and 8c, respectively. The asterisks
822 represent that no light-absorbing component was assumed in the second log-normal
823 distribution of $j = 2$ in Eq. (3).

824

825 Table 3 Estimated σ_{ts}^{λ} ($\times 10^{-6}$ m^{-1}), σ_a ($\times 10^{-6}$ m^{-1}), *SSA*, *AE*, and *p* in polluted and

826 pristine air masses.

Model	Property	Wavelength nm	Polluted air		Pristine air			
			30.5°N - 29.5°N		17.5°N - 16.0°N		14.5°N - 13.5°N	
Column	σ_{ts}^{λ}	450	50.00		32.51		34.76	
		550	36.42		32.37		35.14	
		700	24.34		31.66		34.59	
	σ_a	565	3.44		0.175		0.348	
	SSA	550	0.914		0.995		0.990	
	AE	450 - 550	1.58		0.02		-0.05	
		450 - 700	1.63		0.06		0.01	
		550 - 700	1.67		0.09		0.07	
	p		3.34×10^{-3}		1.20×10^{-5}		2.88×10^{-4}	
log-normal			GSC[a]	GDC[a]	GSC[b]	GDC[b]	GSC[c]	GDC[c]
	σ_{ts}^{λ}	450	49.40	49.84	32.92	31.73	34.98	35.09
		550	36.33	36.73	32.73	31.62	35.17	35.22
		700	23.98	24.10	32.07	31.11	34.80	34.83
	σ_a	565	3.43	3.45	0.171	0.173	0.358	0.349
	SSA	550	0.914	0.914	0.995	0.995	0.990	0.990
	AE	450 - 550	1.53	1.52	0.03	0.02	-0.03	-0.02
		450 - 700	1.64	1.64	0.06	0.04	0.01	0.02
		550 - 700	1.72	1.75	0.09	0.07	0.04	0.05
	p		1.38×10^{-3}	2.64×10^{-3}	5.50×10^{-5}	6.37×10^{-4}	1.81×10^{-3}	2.07×10^{-3}

827

828 GSC and GDC are acronyms of green solid curve and green dashed curve in Fig. 8,

829 respectively. a, b, and c represent curves in Figs. 8a, 8b, and 8c, respectively.